BIOLOGICAL CRYSTALLOGRAPHY

ISSN 1399-0047

Controlled crystal dehydration triggers a space-group switch and shapes the tertiary structure of cytomegalovirus immediate-early 1 (IE1) protein

Stefan Klingl,[a] Myriam Scherer,[b] Thomas Stamminger[b] and Yves A. Muller[a]*

[a]Division of Biotechnology, Department of Biology, Friedrich-Alexander University Erlangen-Nuremberg, Henkestrasse 91, 91052 Erlangen, Germany, and [b]Institute for Clinical and Molecular Virology, Friedrich-Alexander University Erlangen-Nuremberg, Schlossgarten 4, 91054 Erlangen, Germany. *Correspondence e-mail: yves.muller@fau.de

Received 12 January 2015
Accepted 6 May 2015

Edited by T. O. Yeates, University of California, USA

Keywords: viral effector protein; humidity-control device; improved scattering and diffraction; lattice symmetry increase; free-mounting system; space-group transition.

PDB reference: immediate-early 1 protein of rhesus macaque cytomegalovirus, 4wic

Supporting information: this article has supporting information at journals.iucr.org/d

Cytomegalovirus immediate-early 1 (IE1) protein is a key viral effector protein that reprograms host cells. Controlled dehydration experiments with IE1 crystals not only extended their diffraction limit from 2.85 to 2.3 Å resolution but also triggered a monoclinic to tetragonal space-group transition with only minor alterations in the unit-cell parameters. An analysis of the pre-dehydration and post-dehydration crystal structures shows how dehydration rearranges the packing of IE1 molecules to meet the unit-cell constraints of the higher lattice symmetry. The transition from $P2_1$ to $P4_3$ reduces the number of copies in the asymmetric unit from four to two, and molecules previously related by noncrystallographic symmetry merge into identical crystallographic copies in the tetragonal space group. At the same time, dehydration considerably alters the tertiary structure of one of the two remaining IE1 chains in the asymmetric unit. It appears that this conformational switch is required to compensate for a transition that is assumed to be unfavourable, namely from a highly preferred to a rarely observed space group. At the same time, the dehydration-triggered molecular reshaping could reveal an inherent molecular flexibility that possibly informs on the biological function of IE1, namely on its binding to target proteins from the host cell.

1. Introduction

Immediate-early 1 (IE1) protein is a key effector protein in cytomegaloviruses and is abundantly expressed during the lytic replication cycle. IE1 consists of a globular core domain, $IE1_{CORE}$, which is flanked by an intrinsically disordered N-terminal and C-terminal region (Scherer *et al.*, 2014; Krauss *et al.*, 2009). Individual regions and domains of IE1 convey distinct functions to the protein (Scherer & Stamminger, 2014). Whereas the terminal regions are important for nuclear import, interaction with the signal transducer and activator of transcription (STAT) protein and histone binding/chromatin tethering, $IE1_{CORE}$ is required for targeting the promyelocytic leukaemia (PML) protein of the host cell. $IE1_{CORE}$-triggered deSUMOylation of PML represents a key step in overcoming the PML-linked intrinsic immune mechanism (Ahn *et al.*, 1998; Ahn & Hayward, 1997; Lee *et al.*, 2004; Wilkinson *et al.*, 1998; Scherer *et al.*, 2014). $IE1_{CORE}$ also participates in the interaction of IE1 with retinoblastoma-like protein 1 (p107), a tumour suppressor and a regulator of cell proliferation and the cell cycle (Johnson *et al.*, 1999; Poma *et al.*, 1996).

The first insight into the structure of IE1 was obtained by the recent crystal structure determination of $rhIE1_{CORE}$, namely of a segment that covers residues 36–395 of IE1 from rhesus macaque cytomegalovirus (Scherer *et al.*, 2014). The tertiary structure of $rhIE1_{CORE}$ is best described as consisting

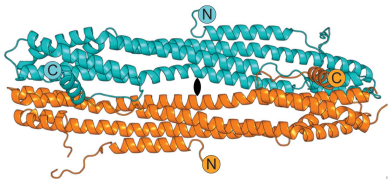

© 2015 International Union of Crystallography

of a single domain. The all-α-helical, elongated, femur-like domain is capped at its two ends by an N-terminal and a C-terminal head region (Scherer *et al.*, 2014; Fig. 1*a*). Surprisingly, no fold similarity could be detected between rhIE1$_{CORE}$ and any other protein from the Protein Data Bank at the time of publication; hence, it was concluded that rhIE1$_{CORE}$ displays a novel protein fold (Rose *et al.*, 2015; Scherer *et al.*, 2014).

Crystallography is one of the most powerful techniques for analyzing the structures and mechanisms of macromolecules. However, the crystallization of biological macromolecules remains challenging as crystal growth is often hampered by the presence of large disordered regions, conformational heterogeneity and interdomain flexibility as well as impediments to the formation of suitable protein-packing contacts. Whereas many of these issues can be addressed by the production of different truncation and mutant variants of the protein of interest, additional techniques exist that can be applied post protein crystallization in an attempt to improve crystal quality. These include the optimization of cryoconditions, crystal soaking with a stabilizing ligand and crystal cross-linking (Heras & Martin, 2005; Newman, 2006). Moreover, dehydration and/or rehydration of protein crystals has proven to be beneficial for extending the diffraction limits of crystals in many cases (Russo Krauss *et al.*, 2012). While protocols exist to achieve dehydration by plain air drying, the inclusion of dehydrating agents and the use of saturated salt solutions to produce an osmotic effect (Perutz, 1946; Bragg & Perutz, 1952; Huxley & Kendrew, 1953; Schick & Jurnak, 1994; Heras *et al.*, 2003), more advanced setups such as a free-mounting systems or humidity-control devices provide a reproducible means of investigating dehydration effects (Kiefersauer *et al.*, 1996, 2000; Sanchez-Weatherby *et al.*, 2009; Bowler *et al.*, 2015). These devices allow precise control of the humidity of the atmosphere that surrounds the crystal while at the same time monitoring changes in the diffraction power of the crystals *via* the online collection of X-ray diffraction images. Moreover, these techniques allow the detailed characterization of changes in unit-cell parameters, space group, mosaicity, $I/\sigma(I)$ and peak profiles upon dehydration and rehydration of crystals (Russi *et al.*, 2011).

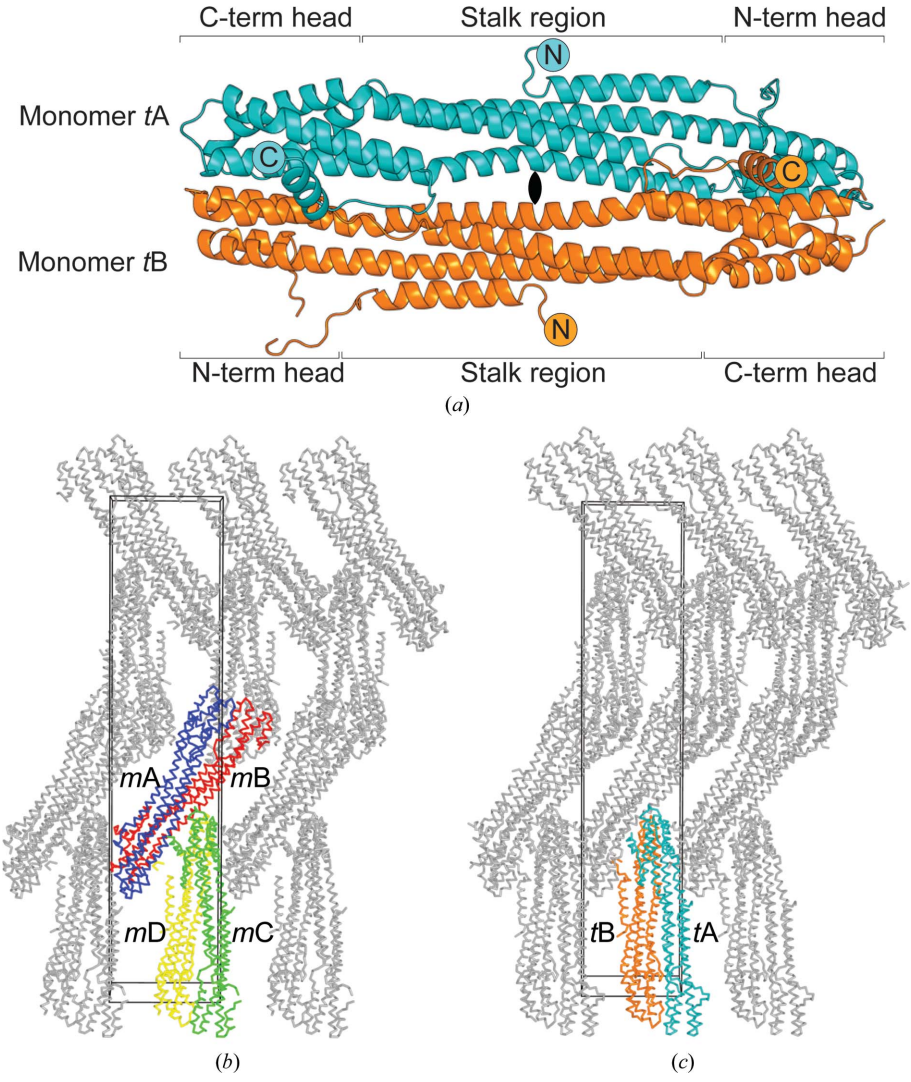

Figure 1
Crystal packing of rhIE1$_{CORE}$ dimers in space groups $P2_1$ and $P4_3$. (*a*) RhIE1$_{CORE}$ forms dimers with C_2 point-group symmetry in both space groups. (*b*) Crystal packing of rhIE1$_{CORE}$ dimers in space group $P2_1$. The four monomers *m*A, *m*B, *m*C and *m*D of the asymmetric unit are shown in blue, red, green and yellow, respectively. (*c*) Crystal packing of rhIE1$_{CORE}$ dimers in $P4_3$ following crystal dehydration. The two molecules *t*A and *t*B of the asymmetric unit are shown in cyan and orange, respectively. In space group $P4_3$ molecules *m*A and *m*C become related by crystallographic symmetry and merge into molecule *t*A. The same holds true for molecules *m*B, *m*D and *t*B.

Here, we describe how this technique has facilitated the structure determination of rhIE1$_{CORE}$. Dehydration of the rhIE1$_{CORE}$ crystals extends their diffraction limit reproducibly and triggers a space-group transition, namely to a lattice system with higher symmetry, while retaining nearly identical unit-cell parameters. At the same time, this space-group change reduces the number of molecules in the crystallographic asymmetric unit and significantly sculpts the tertiary structure of one of the two remaining copies of rhIE1$_{CORE}$ present in the asymmetric unit.

2. Methods

2.1. Protein expression and crystallization

An *Escherichia coli* codon-optimized version of the IE1 gene of rhesus macaque cytomegalovirus (RhCMV, isolate 180.92; UniProt ID Q2FAE9;

Rivailler *et al.*, 2006) was obtained through commercial gene synthesis (GeneArt, Regensburg). The region coding for amino acids 36–395 (rhIE1$_{CORE}$) was cloned into the pGEX-6P-1 vector (GE Healthcare, Uppsala, Sweden) and the protein was expressed in *E. coli* strain BL21(DE3) at 30°C in LB medium as a GST-tagged fusion protein and purified as described previously (Scherer *et al.*, 2014). Briefly, GST-tagged rhIE1$_{CORE}$ protein was isolated from the lysate using a Glutathione Sepharose column (GE Healthcare) and the tag was removed by proteolytic cleavage and separated from the rhIE1$_{CORE}$ protein by a second glutathione affinity purification. Reductive lysine methylation was performed using formaldehyde and dimethylamine–borane (Walter *et al.*, 2006). After a final size-exclusion chromatography step (HiLoad Superdex 200 16/60, GE Healthcare), the protein was concentrated to 20 mg ml^{-1} and dialysed against 25 m*M* Tris–HCl, 15 m*M* DTT, 1 m*M* EDTA pH 7.4.

Crystallization was achieved using a hanging-drop vapour-diffusion setup in combination with microseeding. Crystallization droplets were set up with either 1 or 2 µl protein solution mixed with 1 µl reservoir solution supplemented with microseeds and the droplets were equilibrated over 700 µl reservoir solution at 19°C. The reservoir solution consisted of 400 m*M* magnesium formate, 15%(*w*/*v*) PEG 3350.

2.2. Dehydration experiments

All dehydration experiments were performed with an HC1c crystal-humidifier device (Maatel, Vorreppe, France) installed on MX beamline 14.3 at the BESSY II synchrotron in Berlin (Mueller *et al.*, 2012; Sanchez-Weatherby *et al.*, 2009; Bowler *et al.*, 2015). The initial relative humidity (RH) of the crystals was determined to be 98% by monitoring the diameter of a drop of reservoir solution in the humidifier stream (Sanchez-Weatherby *et al.*, 2009). The crystals were harvested with LithoLoop Meshes (Molecular Dimensions Inc., Altamonte Springs, USA) of either 0.2 or 0.4 mm in diameter with 40 µm mesh size. The crystals used in the dehydration experiments were between 300 and 500 µm in length and 150 to 200 µm in width and thickness. Larger crystals showed an increased tendency to crack during the dehydration process. The crystals were mounted manually and excessive mother liquor was removed using a paper wick. The scattering quality of the crystals was monitored at different RH intervals *via* single X-ray exposures. The images were visually inspected and evaluated using *iMosflm* to monitor changes in the diffraction power, unit-cell parameters, space group, mosaicity and the number of spots with $I/\sigma(I) > 5$ (Battye *et al.*, 2011). Initial dehydration tests were performed with RH decrements of 2% per step and 4 min equilibration periods between RH steps to allow the crystals to accommodate the changes in humidity. In all tests the diffraction power maxed out at 86% RH and decreased again when the RH was further reduced (to as low as 76% RH). In order to eliminate radiation damage as a source of this decay, crystals were also dehydrated without recording X-ray images between 98 and 86% RH. The maximum scattering power was still reproducibly observed at 86% RH. A slower dehydration regime (allowing equilibration periods of up to 10 min) as well as a more rapid dehydration (4% RH decrements) produced similar improvements in diffraction power. A general problem was the observation that many crystals developed cracks or became bent during the dehydration experiments.

The dehydrated crystal that was used to collect a complete data set was prepared by decreasing the RH from 98 to 86% in 4% steps with 10 min equilibration periods between steps. Single diffraction images were collected at the beginning and the end of the dehydration protocol to verify the diffraction-enhancing effects of the dehydration. The dehydrated crystal was then flash-cooled in liquid nitrogen without additional cryoprotectant and transferred to MX beamline 14.1 at the BESSY II synchrotron for data collection.

Table 1
Data-collection and refinement statistics.

The data-collection statistics for the pre-dehydration crystal have been reported elsewhere together with the statistics and the post-dehydration refined atomic model of rhIE1$_{CORE}$ (Scherer *et al.*, 2014). They are listed here for comparison only. The pre-dehydration model, which was previously used as a preliminary search model for initial phasing of the $P4_3$ data set, was refined to convergence in the present study.

	Pre-dehydration (4wic)	4wid
Data collection		
Space group	$P2_1$	$P4_3$
Unit-cell parameters		
a (Å)	58.0	56.5
b (Å)	278.6	56.5
c (Å)	61.6	276.9
$\alpha = \beta = \gamma$ (°)	90.0	90.0
X-ray source	BESSY MX 14.1, Berlin	BESSY MX 14.1, Berlin
Detector	MAR CCD MX-225	MAR CCD MX-225
Wavelength (Å)	0.9184	0.9184
Resolution (Å)	20–2.85 (2.92–2.85)	49–2.3 (2.37–2.30)
Crystal mosaicity (°)	0.201	0.195
R_{merge} (%)	7.2 (96.5)	6.0 (59.1)
$\langle I/\sigma(I)\rangle$	16.9 (1.7)	16.9 (1.6)
Completeness (%)	99.5 (99.7)	99.3 (93.7)
Multiplicity	3.7	5.9
Refinement		
Resolution (Å)	19.93–2.85	49–2.3
No. of reflections	45137	37710
R_{work}/R_{free} (%)	21.17/25.94	19.73/24.96
No. of atoms		
Total	11177	5833
Protein	11177	5694
Water	—	123
Ligands	—	16
B factors (Å^2)		
Protein	75.3	61.8
Water	—	51.8
Ligands	—	89.5
R.m.s. deviations		
Bond lengths (Å)	0.011	0.008
Bond angles (°)	1.43	1.00

2.3. Structure refinement and validation

The structures of rhIE1$_{CORE}$ in space groups $P2_1$ and $P4_3$ were solved as described previously (Scherer *et al.*, 2014). Initial phases were derived from a multi-wavelength anomalous diffraction (MAD) data set collected from gold-soaked monoclinic crystals. In the monoclinic crystals four monomers

are present in the crystallographic asymmetric unit and these assemble into two rhIE1$_{CORE}$ dimers. An initial atomic model of rhIE1$_{CORE}$ was built and used to phase a higher resolution tetragonal data set collected from dehydrated crystals *via* molecular replacement with *Phaser* (McCoy *et al.*, 2007). Considerable rebuilding and refinement with *Coot* and *PHENIX*, respectively, was required to accommodate the displacement of several secondary-structure elements in the tetragonal crystals (Scherer *et al.*, 2014; Adams *et al.*, 2010; Emsley *et al.*, 2010). As part of the current study, we now refined the atomic structure of rhIE1$_{CORE}$ as observed in the initial monoclinic crystals with *PHENIX* (Adams *et al.*, 2010) to final R_{work} and R_{free} values of 21.17 and 25.94%, respectively (Table 1).

2.4. Model validation and structure analysis

Real-space correlation coefficients (RSCCs) were calculated with *EDSTATS* and r.m.s deviations with *LSQKAB*, both of which are available within the *CCP*4 program suite (Kabsch, 1976; Winn *et al.*, 2011). Illustrations depicting molecules and electron-density maps were created with *PyMOL* (v.1.3r1; Schrödinger) unless otherwise stated. The distributions of the thermal displacement factors (*B* factors) in the rhIE1$_{CORE}$ dimers were visualized using the 'render by attribute' option in *UCSF Chimera* (Pettersen *et al.*, 2004). Changes in the packing of the rhIE1$_{CORE}$ crystal interfaces were analyzed with *QtPISA* (Krissinel & Henrick, 2007). The self-rotation plots were generated with *POLARRFN* from the *CCP*4 package (Kabsch, 1976).

3. Results

3.1. Monoclinic IE1 crystals allowed initial model building

Screening for crystallization conditions of the IE1 proteins from different CMV species yielded either no crystals or only poorly diffracting crystals. Diffraction-quality crystals could only be obtained from a terminally truncated variant of the IE1 protein from rhesus macaque CMV (residues 36–395) and following reductive lysine methylation of the protein sample. Initial crystals were only observed in a single crystallization condition. Despite numerous optimization efforts, including variation of the reservoir composition, pH, temperature, protein concentration and cryoprotectant and microseeding, these crystals only diffracted to a resolution of 3.5 Å on a home X-ray source and to 2.85 Å resolution at the BESSY II synchrotron in Berlin (Fig. 2*a*). In-house room-temperature measurements eliminated cryocooling as a possible cause of the limited scattering. Repeat thawing and freezing (crystal annealing) and crystal cross-linking experiments did also not extend the diffraction limit. Nevertheless, initial phases could be derived from these monoclinic rhIE1$_{CORE}$ crystals *via* MAD experiments. The unit cell of these crystals in space group $P2_1$ is characterized by two shorter axes of almost identical lengths, namely *a* and *c* of 58.0 and 61.6 Å, respectively, and a considerably longer *b* axis of 278.6 Å (Table 1; Fig. 2). As is mandatory for the monoclinic *B* setting the α and γ angles equal 90°; however, it is noteworthy that the β angle (90.9°) deviates only slightly from 90°.

3.2. Controlled dehydration triggers a monoclinic to tetragonal lattice transition

In an attempt to extend the diffraction limit of the monoclinic rhIE1$_{CORE}$ crystals *via* dehydration, the crystals were mounted in the humidifier stream at 98% RH and the humidity was reduced in 2% steps. The diffraction power of the crystals started to significantly increase at about 88% RH and defined changes in the reflection intensities in the diffraction pattern occurred (Fig. 2). Analysis of subsequently recorded partial data sets with *POINTLESS* hinted that the underlying Laue group switched from 2/*m* to 4/*m* in hand with a crystal lattice transition from a monoclinic to a tetragonal space group (Evans, 2006).

The lattice transition became clearly apparent when monitoring the intensities of the reflections along the shortest reciprocal axis (the longest real-space axis), which corresponds to the *b** axis in the monoclinic and to the *c** axis in the tetragonal lattice system (Fig. 2*c*). Before dehydration only every second reflection in the direction of the *b** axis (0*k*0 reflections) was present, as expected for space group $P2_1$. Some of these reflections became systematically weaker at around 88% relative humidity, and at 86% relative humidity, where the crystals diffracted best, only every fourth reflection along this axis remained present, which is in agreement with a transition of the 2_1 screw axis to a 4_3 (or 4_1) screw axis and a concurrent change in the lattice system (Fig. 2*c*).

A complete data set collected from the dehydrated crystals could be indexed, merged and solved in space group $P4_3$. This data set extended to a resolution of 2.31 Å (Fig. 2*b*), which corresponds to an increase in resolution of about 0.54 Å when compared with the best data set collected from nondehydrated monoclinic crystals (Table 1). Interestingly, dehydration had little effect on the crystal mosaicity (Table 1). The unit-cell parameters of the tetragonal crystals are altered such that the long axis as well as one of the short axes of the monoclinic crystals are reduced by 1.5–1.7 Å, while the second short axis is shortened more significantly, namely by 5.1 Å (Fig. 2*c*), corresponding to a reduction in length of 8.3%. Overall, these changes translate to a reduction in the unit-cell volume of about 11% (995 000 Å^3 in $P2_1$ and 884 000 Å^3 in $P4_3$). The unit cell contains eight rhIE1$_{CORE}$ protein chains in both crystal forms. The Matthews coefficient (Matthews, 1968) is 2.96 Å^3 Da^{-1} for the crystals in space group $P2_1$ (58% solvent content) and 2.62 Å^3 Da^{-1} for those in space group $P4_3$ (53% solvent content).

3.3. An increase in lattice symmetry is accompanied by changes in crystal packing

The extension of the diffraction limit of the dehydrated crystals is accompanied by adjustments in the crystal-packing contacts of rhIE1$_{CORE}$. Whereas such a behaviour has been observed before in similar studies (Awad *et al.*, 2013), in the case of rhIE1$_{CORE}$ the crystal-packing rearrangements

additionally trigger a transition from a primitive monoclinic to a primitive tetragonal space group, and this transition causes a reduction in the number of protein chains present in the crystallographic asymmetric unit. Thus, the composition of the asymmetric unit changes from four copies of rhIE1$_{CORE}$ (hereafter named molecules *m*A, *m*B, *m*C and *m*D) to two copies (*t*A and *t*B) (Fig. 1). More precisely, two rhIE1$_{CORE}$ molecules (here named *m*A and *m*C) which were related by a noncrystallographic symmetry operator in space group $P2_1$ merge into a single copy of rhIE1$_{CORE}$ (here named *t*A) in space group $P4_3$ since the corresponding molecules become related by crystallographic symmetry. The same applies to molecules *m*B and *m*D in the monoclinic crystals, which merge into copy *t*B in the tetragonal structure.

RhIE1$_{CORE}$ forms dimers with C_2 point-group symmetry in both crystal lattices. In these dimers the N-terminal head region of one monomer is juxtaposed with the C-terminal head region of the second monomer and *vice versa* (Fig. 1*a*). Size-exclusion chromatography experiments show that rhIE1$_{CORE}$ elutes at a reduced molecular weight after chemical methylation of surface-exposed lysine residues (data not shown). However, the dimer entity appears to be retained after methylation and at the same time is also present in the biologically active state of IE1 (Scherer *et al.*, 2014). When analyzing the molecular packing, the changes that occur within the rhIE1$_{CORE}$ dimer interface, namely at the dimer interfaces *m*A–*m*B, *m*C–*m*D and *t*A–*t*B, can be discussed separately from those that occur between dimers as a result of the phase

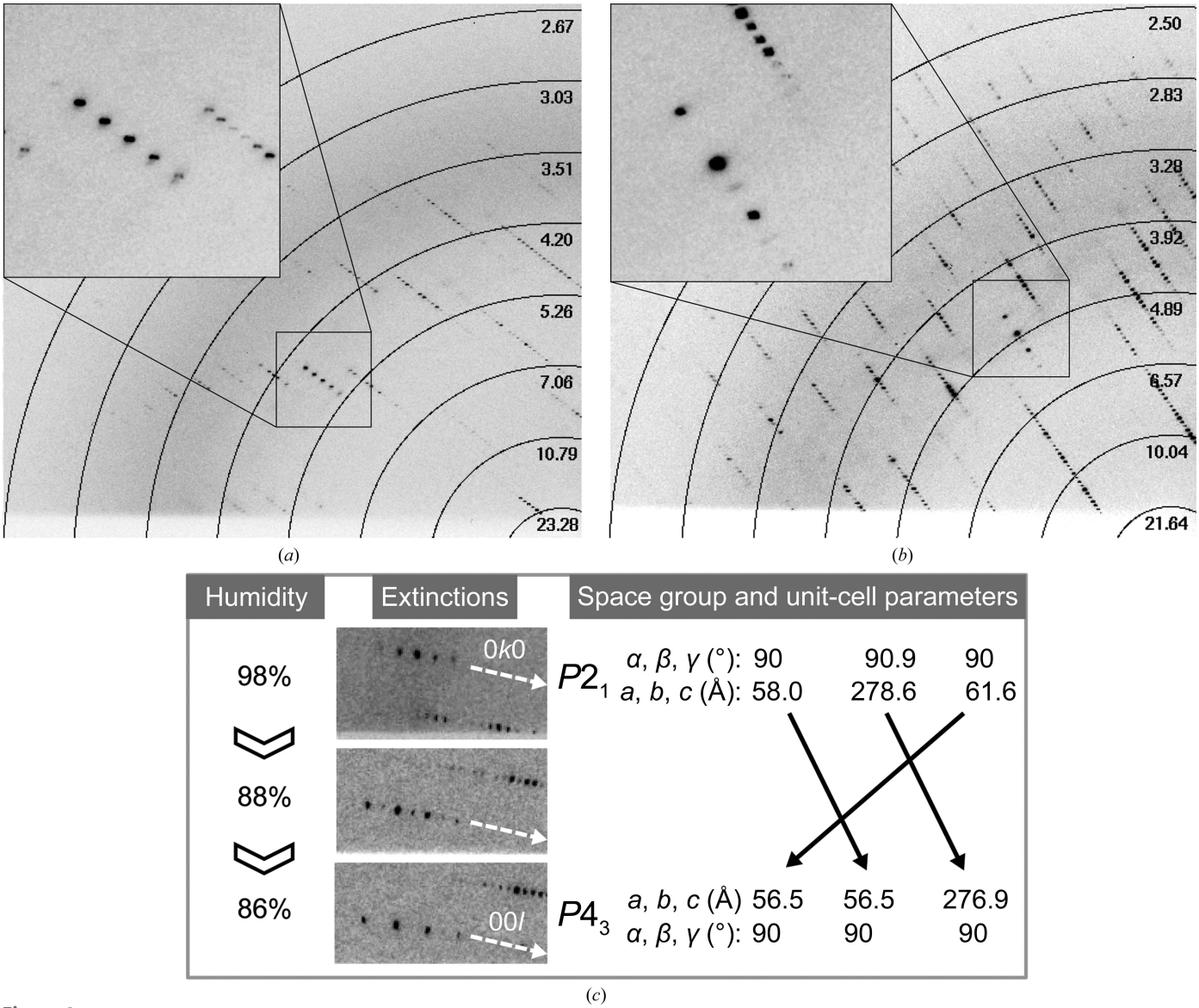

Figure 2
Dehydration of rhIE1$_{CORE}$ crystals extends their diffraction limit and triggers a space-group transition. (*a*) Diffraction image from the starting monoclinic crystals (pre-dehydration). In the inset the systematic extinctions caused by the 2_1 screw axis are highlighted. (*b*) Diffraction image from a tetragonal crystal after dehydration. Systematic extinctions caused by the newly formed 4_3 screw axis are highlighted in the inset. (*c*) Illustration of the humidity-controlled phase transition and the relationship between the unit-cell parameters of the monoclinic and tetragonal crystals.

transition. The high number of local rearrangements in the rhIE1$_{CORE}$ crystals affects both the dimerization interfaces and the crystal-packing contacts.

All four molecules, *m*A to *m*D, in the asymmetric unit of the monoclinic crystals display significant differences in their crystal-packing contacts. The solvent-accessible surface areas buried in packing contacts range from 1500 to 2180 Å^2 per rhIE1$_{CORE}$ protein chain (with an average value of 1860 Å^2) in the monoclinic space group (Table 2). These packing interactions increase after the space-group transition to 2440 and 2760 Å^2 for molecules *t*A and *t*B, respectively (with an average value of 2600 Å^2; Table 2). More detailed observations can be made when visualizing individual surface patches involved in crystal-packing contacts, as illustrated for molecules *m*B and *m*D in Fig. 3. *m*B and *m*D merge into a single crystallographic copy, namely *t*B, after the transition. When viewing the molecules in the orientation depicted in Fig. 3 then it becomes apparent that *m*B and *m*D differ considerably with regard to the surface patches contributed by each molecule to crystal-packing contacts. Following the space-group transition, the new crystal-packing contacts of molecule *t*B only approximately correspond to the sum of the packing contacts seen in *m*B and *m*D, since not only are new packing contacts generated during the transition but the previous contacts are also disrupted (Fig. 3). Overall, the crystal-packing contact area of *m*B increases from 2180 to 2760 Å^2 (a 27% increase), while that of *m*D increases from 1900 to 2760 Å^2 (a 45% increase; Table 2). With respect to all four rhIE1$_{CORE}$ molecules in $P2_1$, the largest increase can be observed for molecule *m*A. Here, the crystal-packing contact area increases from 1500 Å^2 in *m*A to 2440 Å^2 in molecule *t*A (a 63% increase; Table 2).

Table 2
Surface and interface areas of rhIE1 (36–395) before/after crystal dehydration.

	$P2_1$		$P4_3$	$P2_1$		$P4_3$
	*m*A	*m*C	*t*A	*m*B	*m*D	*t*B
No. of residues	349	349	353	341	340	349
ASA† (Å^2)	20730	20350	19940	19600	20070	20340
DIA‡ (Å^2)	2560	2490	3100	2480	2480	3250
CCA§ (Å^2)	1500	1860	2440	2180	1900	2760

† Total accessible surface area of each monomer. ‡ Surface area contributed by each monomer to the dimerization interface. § Total surface area of each monomer involved in crystal-packing contacts with the dimerization interface area exempted.

Table 3
R.m.s. deviations (in Å) between the C$^\alpha$ atoms of the different monomers in the monoclinic and tetragonal asymmetric units.

Values above the diagonal are pairwise r.m.s. deviations obtained upon superposition of all common residues (residues 41–63, 70–73, 79–342 and 346–392). Values below the diagonal are pairwise r.m.s. deviations obtained upon superposition of α-helical regions only as defined in Scherer *et al.* (2014).

	Monoclinic crystals				Tetragonal crystals	
	*m*A	*m*B	*m*C	*m*D	*t*A	*t*B
*m*A		1.92	1.13	1.65	3.12	2.66
*m*B	1.12		1.62	1.52	3.09	1.54
*m*C	1.03	0.92		1.84	2.99	2.23
*m*D	1.17	1.03	1.31		3.40	2.52
*t*A	3.05	2.49	2.86	2.91		2.90
*t*B	2.05	1.34	1.55	2.07	2.13	

3.4. Increased packing interactions reduce local flexibility and improve the definition of atom positions

In order to assess any local effects resulting from the dehydration-induced space-group transition, the *B* factors, together with the real-space correlation coefficients (RSCCs), were plotted per residue for the different monomers before and after dehydration (Fig. 4). Interestingly, the distribution of regions with high *B* factors is highly dissimilar between the different rhIE1$_{CORE}$ chains in monomers *m*A to *m*D, despite the observation that all molecules retain a similar overall main-chain conformation (Table 3). At the same time, the *B*-factor distribution of monomers *m*A and *m*C, as well as *m*B and *m*D, appear to be correlated (Fig. 4). Thus, the region surrounding residue 260 displays elevated *B* factors in molecule *m*C and to a lesser extent also in *m*A,

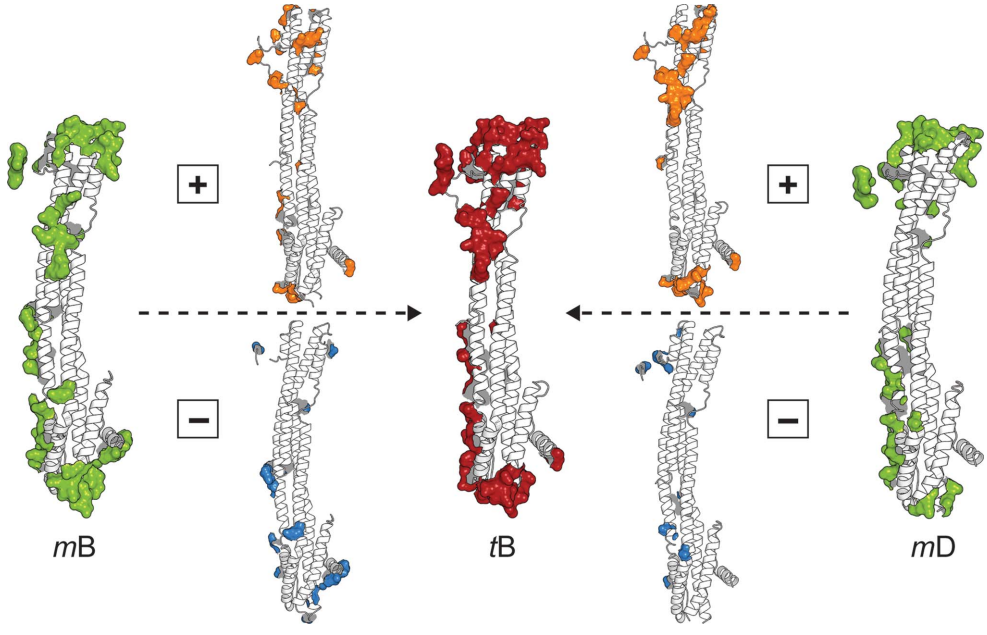

Figure 3
Dehydration-induced changes in the crystal-packing contacts exemplified for the transition of molecules *m*B and *m*D (space group $P2_1$) to molecule *t*B (space group $P4_3$). The crystal-packing contacts of molecules *m*B and *m*D (in green) differ in space group $P2_1$ but are identical in space group $P4_3$ (molecule *t*B, contacts in red). Individual contacts are either newly formed (indicated in orange, plus sign) or disrupted (indicated in cyan, minus sign) during the phase transition and the merging of molecules *m*B and *m*D into *t*B.

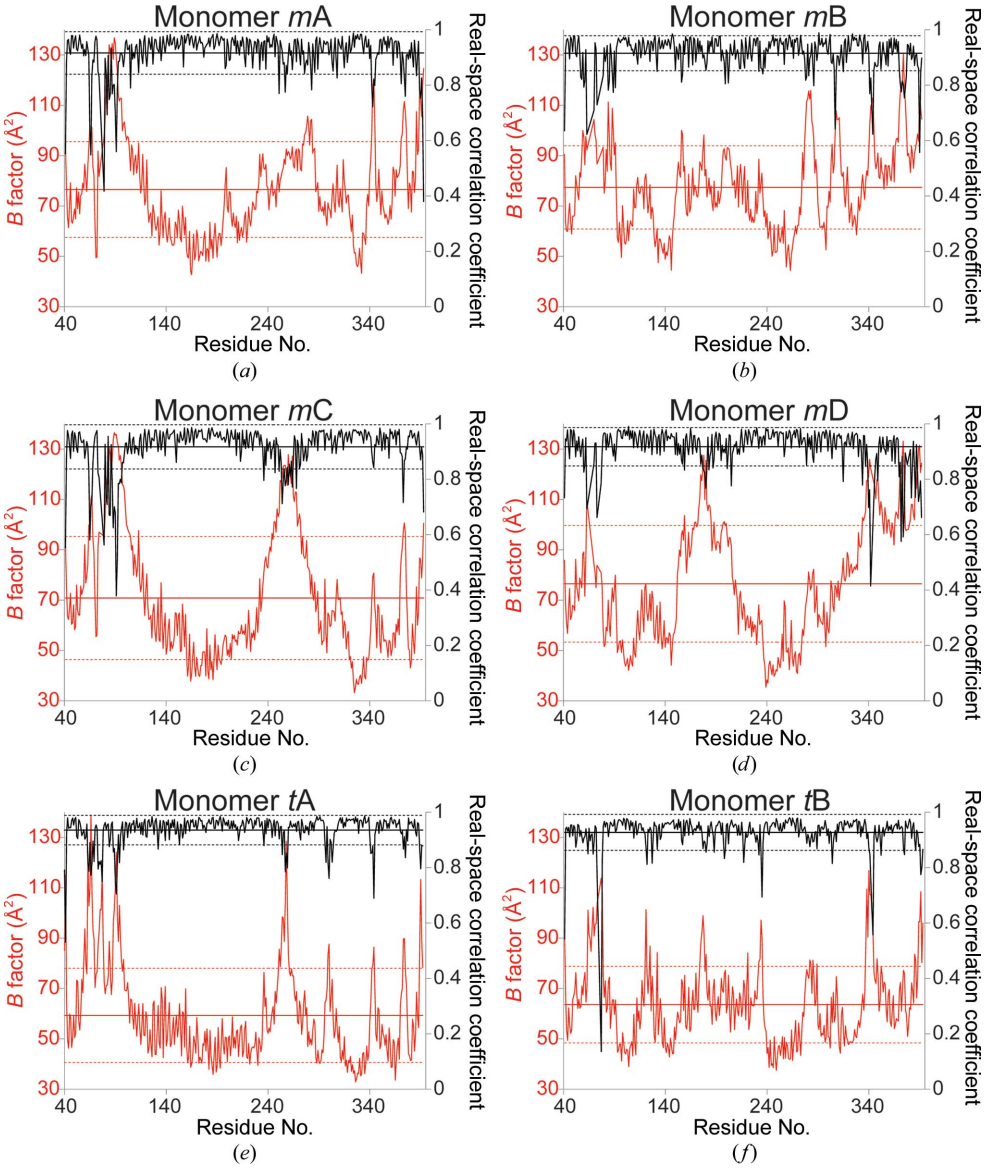

Figure 4
RSCC (in black) and *B*-factor (in red) distributions of the four rhIE1$_{CORE}$ molecules in space group $P2_1$ (*a*–*d*) and the two rhIE1$_{CORE}$ molecules in space group $P4_3$ (*e*, *f*). Mean values are indicated by solid black and red lines. Mean values plus/minus one standard deviation are shown by dashed lines.

whereas residues 170–190 display high *B* factors only in *m*B and *m*D. The reason for this behaviour becomes apparent when mapping the *B* factors onto the structure of the different rhIE1$_{CORE}$ dimers (Fig. 5). Thus, it appears that within each dimer only one pole of the elongated dimer displays high *B* factors. Since rhIE1$_{CORE}$ dimerization occurs in a head-to-tail fashion, regions of high *B*-factor values arise from the juxtaposition of the N-terminal head region of *m*A (or likewise *m*C) with the C-terminal head region of *m*B (or *m*D), hence the observed pairwise similarities between the *B*-factor distribution in these molecules (Figs. 5*a* and 5*b*).

After the phase transition, the noncrystallographically related molecules *m*A and *m*C become related by crystallographic symmetry in the tetragonal space group (molecule *t*A), and therefore these molecules display identical *B*-factor distributions in the post-dehydration crystals. The same applies to molecules *m*B, *m*D and *t*B. Molecules *t*A and *t*B remain crystallographically dissimilar; however, any differences in the thermal mobility distributions of these molecules appear considerably less pronounced than in molecules *m*A to *m*D from the pre-dehydration structure (Figs. 4*e*, 4*f* and 5*c*).

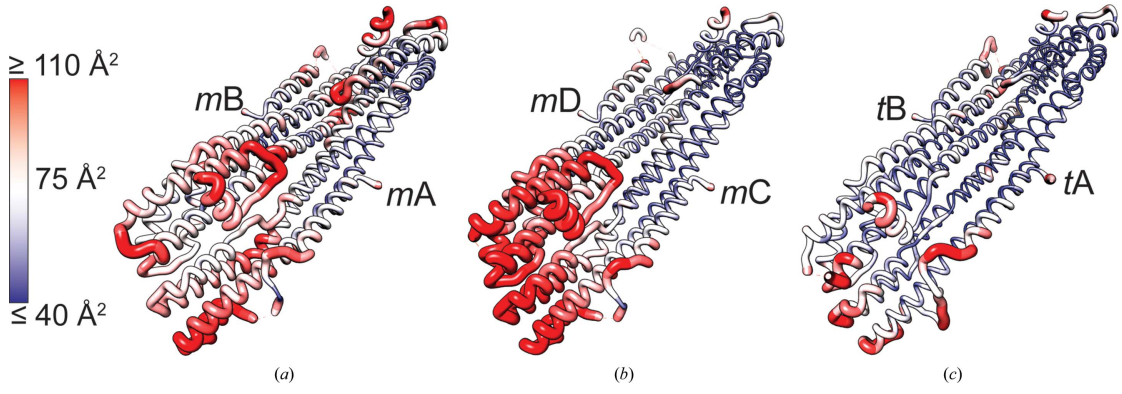

Figure 5
Cartoon representations of all three rhIE1$_{CORE}$ dimers coloured according to their *B* factors. (*a*, *b*) Dimers *m*A–*m*B and *m*C–*m*D from the monoclinic crystals and (*c*) dimer *t*A–*t*B from the tetragonal crystals. Segments with high (110 Å^2 and above) and low (40 Å^2 and lower) *B* factors are coloured red and blue, respectively. Regions with high *B* factors cluster predominantly at one pole of the dimer. This asymmetric distribution is most obvious in the case of dimer *m*C–*m*D (*b*).

A number of segments that are distant from each other in the pre-dehydration structure participate in intermolecular protein interactions in the post-dehydration tetragonal space group as a consequence of the reduction of the unit-cell volume. As a result of these newly formed interactions, these segments become better defined by their local electron density (Fig. 6). For example, the short helix H2 forms neither tight intramolecular nor intermolecular interactions in the monoclinic crystals and is characterized by blurred electron density for its main-chain and side-chain atoms. In the post-dehydration structure the intermolecular distance between H2 of monomer *m*B and H6 from a neighbouring molecule is reduced from about 11 to 7 Å (Figs. 6*a* and 6*b*). The same holds true for helix H2 of monomer *m*A. Here, the distance between helix H2 and helix H1 from an adjacent chain is shortened even further, namely from 14 to 7 Å (Figs. 6*c* and 6*d*). In both cases the newly formed interactions result in better defined electron density for helix H2 and for all contacting helices.

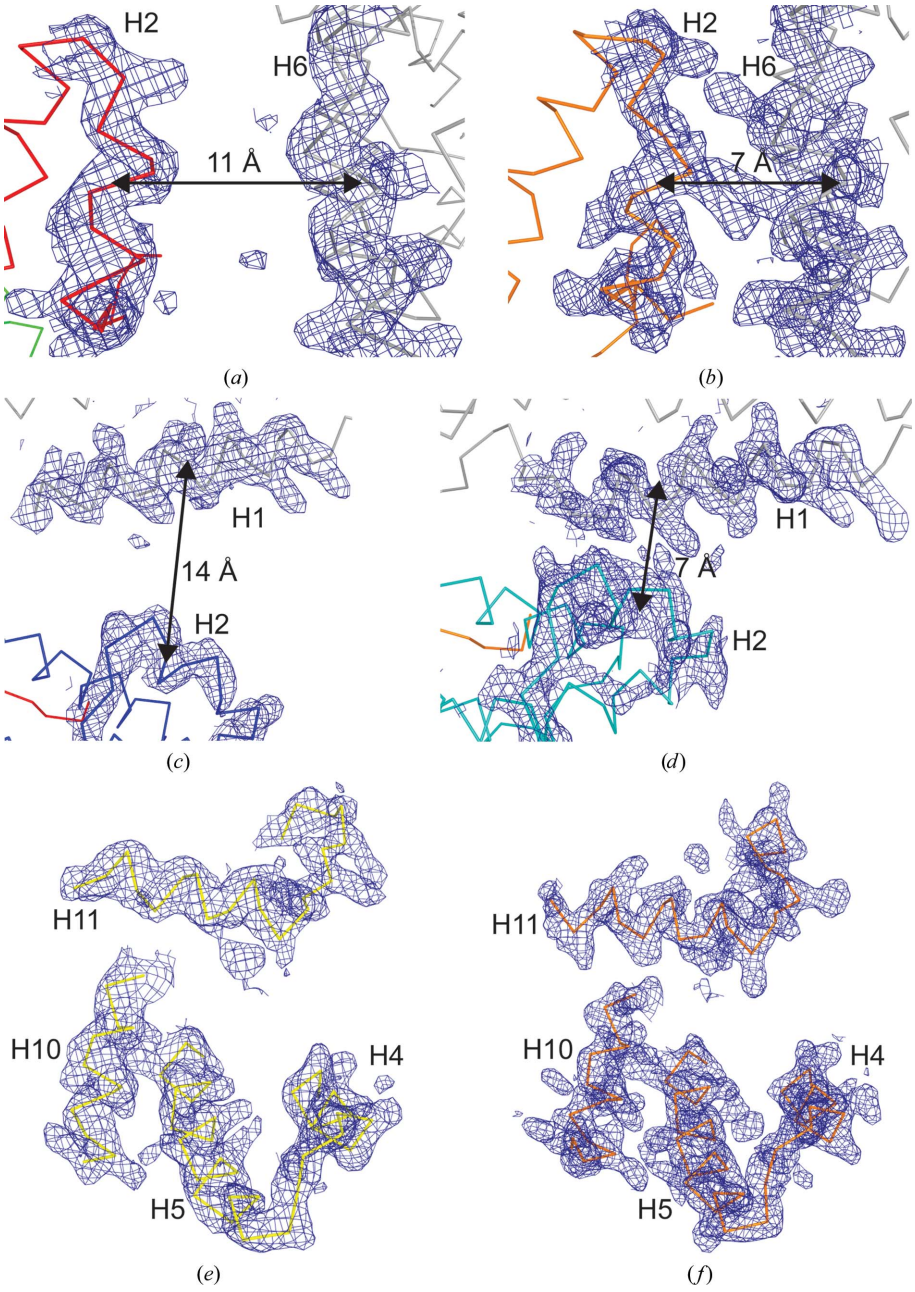

Figure 6
Comparison of electron densities from the pre-dehydration structure (*a*, *c*, *e*) with the corresponding regions from the post-dehydration structure (*b*, *d*, *f*). (*a*) H2 from *m*B and H6 from the closest symmetry mate from the monoclinic structure in comparison to (*b*) H2 from *t*B and H6 from a neighbouring molecule in the tetragonal space group. (*c*) H2 from *m*A and H1 from a symmetry-related molecule in comparison to (*d*) H2 of *t*A as well as H1. (*e*) Pole of the dimer *m*C–*m*D that displays high *B* factors in the monoclinic structure in comparison to (*f*) the corresponding *t*A–*t*B dimer pole in the tetragonal structure. The $2mF_o - DF_c$ maps shown in blue are contoured at 1σ and displayed within a radius of 2.5 Å around selected model atoms.

As discussed above, one pole of the *m*C–*m*D dimer is poorly defined and displays very high *B* factors. Several helices, especially H11 and parts of H10 from the C-terminal head region of the *m*D monomer, lack well defined side-chain density (Fig. 6*e*). After dehydration and upon merging of *m*B and *m*D the resulting molecule *t*B forms additional contacts, and as a result the entire region becomes considerably better defined by its electron density (Fig. 6*f*).

When taken together, it becomes clear that the enhanced packing interactions and the increased scattering power of the tetragonal crystals improve the accuracy of the definition of the atom positions. At the same time, the average RSCC is highly similar for the pre-dehydration (0.92) and the post-dehydration (0.93) structure, hinting that both of the atomic models adequately describe the corresponding diffraction data.

3.5. Dehydration and space-group transition reshape the tertiary and quaternary structures of IE1

The tertiary structures of the *m*A to *m*D chains of rhIE1$_{CORE}$ in the pre-dehydration state are very similar. The pairwise r.m.s. deviations between the C$^{\alpha}$ positions of all common residues range from 1.1 to 1.9 Å (1.61 ± 0.25 Å on average; Table 3, Fig. 7). Even lower deviations ranging from 0.9 to 1.3 Å are observed when limiting the comparison to α-helical secondary-structure elements only (1.10 ± 0.12 Å on average; Table 3). However, it should be noted that owing to the 2.85 Å resolution limit of the monoclinic crystals NCS restraints were applied during model refinement, and this certainly contri-

butes to the low r.m.s. deviations between rhIE1$_{CORE}$ chains in this space group (Table 1).

Surprisingly, upon dehydration we not only observe a space-group transition and an increase in the lattice symmetry but also the emergence of a pronounced shape difference in rhIE1$_{CORE}$, namely the introduction of an extensive kink in the segment that interconnects helices H8 and H9 in one of the two molecules *t*A and *t*B in the asymmetric unit of the tetragonal crystals (Fig. 7). This kink not only alters the location of helix H9 in molecule *t*A but also considerably shifts the adjacent helices H1, H3 and H6 that pack against helix H9 in the stalk region (Figs. 7*b* and 7*d*). At the same time, the main-chain traces in the head regions of molecule *t*A seem to be unaffected by the introduction of the kink. This kink is only introduced into molecule *t*A since the main-chain trace of molecule *t*B remains highly similar to that of the previous molecules *m*A to *m*D (Fig. 7). This is also reflected in the calculation of r.m.s. deviations, which shows that molecule *t*B resembles molecules *m*A to *m*D more closely than molecule *t*A irrespective of whether α-helical secondary-structure elements only or all common C$^{\alpha}$ positions are compared (Table 3).

As a consequence of this dehydration-induced molecular reshaping of molecule *t*A, the dimer interface area between molecules *t*A and *t*B significantly increases. Whereas in the monoclinic crystals an average of 2503 Å^2 is contributed by molecules *m*A to *m*D to the dimer interface, this area increases to 3175 Å^2 for molecules *t*A and *t*B in the tetragonal crystals (Table 2). Thus, dehydration not only increases the crystal-packing contacts between rhIE1$_{CORE}$ dimers but also reshapes the trace of the main-chain conformation of *t*A and as a consequence leads to a 27% increase in the dimerization interface included in the quaternary structure of rhIE1$_{CORE}$. However, with the exception of a single report on DNA crystals (see below), we are not aware of any other controlled dehydration experiment in which dehydration reshaped a well ordered region of the tertiary structure of the crystallized macromolecule to such an extent (Hall *et al.*, 2014).

4. Discussion

Improved scattering upon crystal dehydration has been observed in a number of cases [some of these are summarized in Russo Krauss *et al.* (2012) and Heras *et al.* (2003)]. While in early accounts dehydration was achieved either *via* the osmotic effect of a crystal soaking solution or upon brief blocking of the 100 K cryostream (crystal annealing), recent studies make use of free-mounting systems that allow controlled reduction of the humidity surrounding the crystals and therefore controlled dehydration (Kiefersauer *et al.*, 1996; Sanchez-Weatherby *et al.*, 2009). Dehydration induces a reduction of the crystal solvent content in all cases reported so far. Often, this is directly reflected by a diminution in the length of the cell axes (see, for example, Esnouf *et al.*, 1998). Alternatively, reduction of the solvent content can also be paralleled by a space-group transition (Weiss & Hilgenfeld, 1999; Heras *et al.*, 2003). However, the space-group transition and the concomitant changes in the packing of the protein molecules can often not be analyzed in full detail because of poor scattering of the crystals prior to dehydration (Heras *et al.*, 2003; Oliete *et al.*, 2013).

A number of observations render the dehydration of rhIE1$_{CORE}$ crystals particularly interesting. Not only was it possible to derive detailed atomic models of rhIE1$_{CORE}$ in the pre-dehydration and post-dehydration states, but dehydration of rhIE1$_{CORE}$ also triggers an unusual space-group transition that is characterized by an increase in the lattice symmetry while the unit-cell parameters are nearly retained. As a consequence of the transition from the monoclinic space group $P2_1$ to the tetragonal space group $P4_3$, the number of molecules in the asymmetric unit is reduced from four (*m*A to *m*D) to two (*t*A and

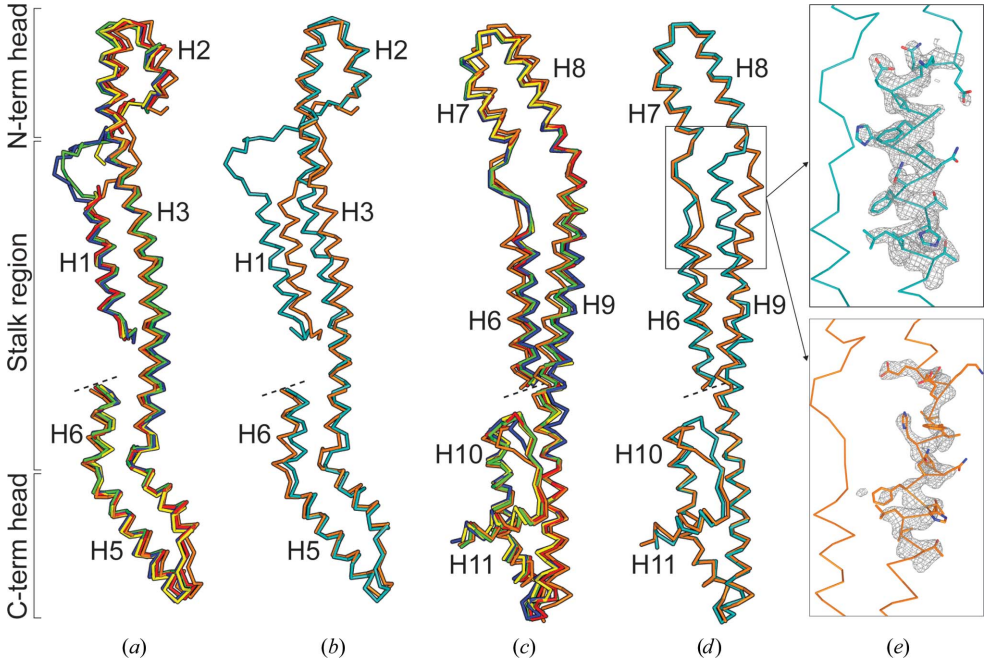

Figure 7
Dehydration and concomitant space-group transition reshapes the tertiary structure of rhIE1$_{CORE}$. (*a*) Superposition of the N-terminal moieties of all *m* chains and of *t*B. (*b*) Superposition of the N-terminal moieties of *t*A and *t*B. (*c*) Superposition of the C-terminal moieties of all *m* chains and of *t*B. (*d*) Superposition of the C-terminal moieties of *t*A and *t*B. (*e*) Insets displaying the Z-like kink in the segment that connects H8 and H9 in molecule *t*A (top) and the identical region in *t*B (bottom). The C$^{\alpha}$ ribbons of the different chains are colour-coded as in Fig. 1. The simulated-annealed OMIT $mF_o - DF_c$ electron-density map is shown in grey, is contoured at 3σ and is displayed within 3 Å of selected atoms.

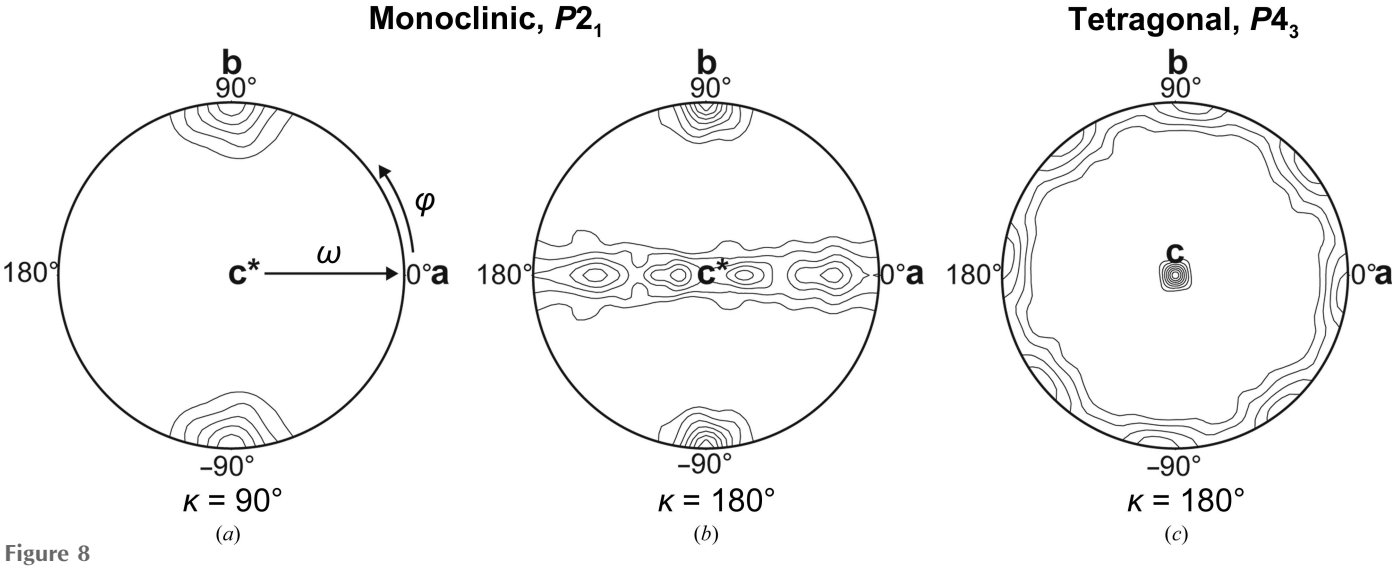

Figure 8
Self-rotation functions calculated from the diffraction data sets of (*a*, *b*) the pre-dehydrated monoclinic crystals and (*c*) the post-dehydrated tetragonal crystals.

*t*B). Hence, molecules previously related by noncrystallographic symmetry in space group $P2_1$ become related by crystallographic symmetry in space group $P4_3$. To our knowledge, such an increase in lattice symmetry with a concomitant reduction in the number of molecules in the asymmetric unit has so far not been reported as the result of a controlled dehydration experiment.

An important constraint has to be fulfilled in order to enable an increase in lattice symmetry from $P2_1$ to $P4_3$. The packing of the different molecules in the lower symmetry space group has to already resemble the packing of the molecules in the higher symmetry lattice. At the same time, dehydration-triggered effects have to enable a readjustment of the molecular packing so that all of the geometric constraints that define the higher symmetry space group are satisfied. In the case of rhIE1$_{\rm CORE}$ the shifts occurring in the lengths of the *a* and *c* axes (58.0 and 61.6 Å) of the monoclinic crystals have to give rise to identical *a* and *b* axes (both 56.0 Å) as required in a tetragonal Bravais lattice. While the β angle is only slightly reduced from 90.9 to 90°, the shift occurring in the *c* axis amounts to as much as 5.6 Å. A self-rotation function calculated from the diffraction data for the monoclinic crystals already reveals the presence of a fourfold rotational symmetry that relates the different orientations of the molecules in the asymmetric unit in the monoclinic crystals and which translates into a 4_3 screw axis in the tetragonal crystals (Figs. 8*a* and 8*b*).

Interestingly, the noncrystallographic rotational symmetry that is apparent from the self-rotation function calculated from the monoclinic data is not limited to a fourfold rotational symmetry oriented parallel to the crystallographic 2_1 screw axis but also reveals the presence of additional noncrystallographic twofold rotations that are oriented perpendicular to the fourfold rotational axis. Thus, the different orientations of the eight molecules in the monoclinic unit cell are in line with symmetry of point group 422. This arrangement is retained in the tetragonal crystal lattice, as is obvious from the self-rotation function calculated from the tetragonal data (Fig. 8*c*). At the same time, the inclination of the additional noncrystallographic twofold or 2_1 axes with respect to the unit-cell axes precludes the presence of a space-group symmetry that would exceed space group $P4_3$. This is also in line with the observation that the diffraction data collected from the tetragonal crystals only adhere to Laue symmetry group 4/*m* and not 4/*mmm*.

When searching the Protein Data Bank it becomes apparent that considerably more macromolecules crystallize in space group $P2_1$ than in space group $P4_3$ (15.6 *versus* 0.6% of all entries; status at December 2014; Rose *et al.*, 2015), which is fully in line with an earlier survey (Wukovitz & Yeates, 1995). Although the presence of multiple copies of protein chains in the asymmetric unit of the monoclinic and tetragonal crystals of rhIE1$_{\rm CORE}$ makes it difficult to directly apply the entropy model proposed by Wukovitz and Yeates to explain the observed space-group preferences (Wukovitz & Yeates, 1995), it seems obvious that in the case of rhIE1$_{\rm CORE}$ the packing of four copies in the asymmetric unit of the monoclinic crystals allows more degrees of freedom than the packing of two copies in the tetragonal crystals. Thus, crystal dehydration triggers an apparently unfavourable transition from an initially favoured monoclinic space group to a considerably less frequently observed tetragonal space group. Interestingly, in rhIE1$_{\rm CORE}$ this unfavourable transition appears to be compensated by the emergence of a dissimilarity in the tertiary structure of rhIE1$_{\rm CORE}$, namely the introduction of a kink in the segment that connects helices H8 and H9 in molecule *t*A, while no such change occurs in *t*B.

Previous reports of dehydration experiments mostly described the occurrence of small rearrangements in the studied macromolecules such as the repositioning of loop regions or minor conformational changes in the well defined protein cores (Fratini *et al.*, 1982; Madhusudan *et al.*, 1993;

Bell, 1999; Harata & Akiba, 2007; Sen *et al.*, 2013). Another class of reported changes encompasses disorder-to-order transitions triggered by the formation of new crystal contacts. In the case of bovine mitochondrial F1-ATPase, disordered parts of the $\gamma\delta\varepsilon$-subunit, for example, become well defined after dehydration without the occurrence of major main-chain conformational changes in the six α- and β-subunits (Bowler *et al.*, 2006). Similar observations have been made with crystals of biotin protein ligase and glypican-1 (Gupta *et al.*, 2010; Awad *et al.*, 2013). Here, the core regions of the proteins also deviated only little between the hydrated and dehydrated structures.

Such an extensive dehydration-triggered conformational switch as observed here for the ordered core of rhIE1 has to our knowledge so far only been reported for a DNA fragment (Hall *et al.*, 2014). In this latter case the DNA fragment switches between two well characterized biological conformations, namely from a pure B conformation to a partial A conformation. It is therefore tempting to propose that in rhIE1$_{\rm CORE}$ the observed conformational switch also does not occur fortuitously but is testimony to an inherent structural flexibility that could be important for the biological function of rhIE1$_{\rm CORE}$. More precisely, the interaction of rhIE1$_{\rm CORE}$ with PML possibly relies on the direct interaction of rhIE1$_{\rm CORE}$ with the coiled-coil domain of PML, and this might require rearrangements in the all-helical domain of rhIE1$_{\rm CORE}$ (Scherer *et al.*, 2014). Thus, dehydration experiments such as those conducted with rhIE1$_{\rm CORE}$ might not only help in improving the resolution of crystal structures but might also be able to provide experimental insight into the inherent flexibility of the studied macromolecules and thereby help to inform us on how these molecules exert their biological function.

Acknowledgements

We would like to thank M. Weiss and U. Mueller from Helmholtz-Zentrum Berlin for help with the crystal-dehydration setup at MX beamline 14.3 at the BESSY II synchrotron, diffraction data collection and discussion. This work was supported by the Deutsche Forschungsgemeinschaft (DFG), SFB796 (projects A3 and B3).

References

Adams, P. D. *et al.* (2010). *Acta Cryst.* D**66**, 213–221.
Ahn, J.-H., Brignole, E. J. & Hayward, G. S. (1998). *Mol. Cell. Biol.* **18**, 4899–4913.
Ahn, J.-H. & Hayward, G. S. (1997). *J. Virol.* **71**, 4599–4613.
Awad, W., Svensson Birkedal, G., Thunnissen, M. M. G. M., Mani, K. & Logan, D. T. (2013). *Acta Cryst.* D**69**, 2524–2533.
Battye, T. G. G., Kontogiannis, L., Johnson, O., Powell, H. R. & Leslie, A. G. W. (2011). *Acta Cryst.* D**67**, 271–281.
Bell, J. A. (1999). *Protein Sci.* **8**, 2033–2040.
Bowler, M. W., Montgomery, M. G., Leslie, A. G. W. & Walker, J. E. (2006). *Acta Cryst.* D**62**, 991–995.
Bowler, M. W., Mueller, U., Weiss, M. S., Sanchez-Weatherby, J., Sorensen, T. L.-M., Thunnissen, M. M. G. M., Ursby, T., Gobbo, A., Russi, S., Bowler, M. G., Brockhauser, S., Svensson, O. & Cipriani, F. (2015). *Cryst. Growth Des.* **15**, 1043–1054.
Bragg, W. L. & Perutz, M. F. (1952). *Acta Cryst.* **5**, 323–328.
Emsley, P., Lohkamp, B., Scott, W. G. & Cowtan, K. (2010). *Acta Cryst.* D**66**, 486–501.
Esnouf, R. M., Ren, J., Garman, E. F., Somers, D. O'N., Ross, C. K., Jones, E. Y., Stammers, D. K. & Stuart, D. I. (1998). *Acta Cryst.* D**54**, 938–953.
Evans, P. (2006). *Acta Cryst.* D**62**, 72–82.
Fratini, A. V., Kopka, M. L., Drew, H. R. & Dickerson, R. E. (1982). *J. Biol. Chem.* **257**, 14686–14707.
Gupta, V., Gupta, R. K., Khare, G., Salunke, D. M., Surolia, A. & Tyagi, A. K. (2010). *PLoS One*, **5**, e9222.
Hall, J. P., Sanchez-Weatherby, J., Alberti, C., Quimper, C. H., O'Sullivan, K., Brazier, J. A., Winter, G., Sorensen, T., Kelly, J. M., Cardin, D. J. & Cardin, C. J. (2014). *J. Am. Chem. Soc.* **136**, 17505–17512.
Harata, K. & Akiba, T. (2007). *Acta Cryst.* D**63**, 1016–1021.
Heras, B., Edeling, M. A., Byriel, K. A., Jones, A., Raina, S. & Martin, J. L. (2003). *Structure*, **11**, 139–145.
Heras, B. & Martin, J. L. (2005). *Acta Cryst.* D**61**, 1173–1180.
Huxley, H. E. & Kendrew, J. C. (1953). *Acta Cryst.* **6**, 76–80.
Johnson, R. A., Yurochko, A. D., Poma, E. E., Zhu, L. & Huang, E. S. (1999). *J. Gen. Virol.* **80**, 1293–1303.
Kabsch, W. (1976). *Acta Cryst.* A**32**, 922–923.
Kiefersauer, R., Stetefeld, J., Gomis-Rüth, F. X., Romão, M. J., Lottspeich, F. & Huber, R. (1996). *J. Appl. Cryst.* **29**, 311–317.
Kiefersauer, R., Than, M. E., Dobbek, H., Gremer, L., Melero, M., Strobl, S., Dias, J. M., Soulimane, T. & Huber, R. (2000). *J. Appl. Cryst.* **33**, 1223–1230.
Krauss, S., Kaps, J., Czech, N., Paulus, C. & Nevels, M. (2009). *J. Virol.* **83**, 12854–12870.
Krissinel, E. & Henrick, K. (2007). *J. Mol. Biol.* **372**, 774–797.
Lee, H.-R., Kim, D.-J., Lee, J.-M., Choi, C. Y., Ahn, B.-Y., Hayward, G. S. & Ahn, J.-H. (2004). *J. Virol.* **78**, 6527–6542.
Madhusudan, Kodandapani, R. & Vijayan, M. (1993). *Acta Cryst.* D**49**, 234–245.
Matthews, B. W. (1968). *J. Mol. Biol.* **33**, 491–497.
McCoy, A. J., Grosse-Kunstleve, R. W., Adams, P. D., Winn, M. D., Storoni, L. C. & Read, R. J. (2007). *J. Appl. Cryst.* **40**, 658–674.
Mueller, U., Darowski, N., Fuchs, M. R., Förster, R., Hellmig, M., Paithankar, K. S., Pühringer, S., Steffien, M., Zocher, G. & Weiss, M. S. (2012). *J. Synchrotron Rad.* **19**, 442–449.
Newman, J. (2006). *Acta Cryst.* D**62**, 27–31.
Oliete, R., Pous, J., Rodríguez-Puente, S., Abad-Zapatero, C. & Guasch, A. (2013). *Acta Cryst.* D**69**, 194–212.
Perutz, M. F. (1946). *Trans. Faraday Soc.* **42**, B187.
Pettersen, E. F., Goddard, T. D., Huang, C. C., Couch, G. S., Greenblatt, D. M., Meng, E. C. & Ferrin, T. E. (2004). *J. Comput. Chem.* **25**, 1605–1612.
Poma, E. E., Kowalik, T. F., Zhu, L., Sinclair, J. H. & Huang, E. S. (1996). *J. Virol.* **70**, 7867–7877.
Rivailler, P., Kaur, A., Johnson, R. P. & Wang, F. (2006). *J. Virol.* **80**, 4179–4182.
Rose, P. W., Prlič, A., Bi, C., Bluhm, W. F., Christie, C. H., Dutta, S., Green, R. K., Goodsell, D. S., Westbrook, J. D., Woo, J., Young, J., Zardecki, C., Berman, H. M., Bourne, P. E. & Burley, S. K. (2015). *Nucleic Acids Res.* **43**, D345–D356.
Russi, S., Juers, D. H., Sanchez-Weatherby, J., Pellegrini, E., Mossou, E., Forsyth, V. T., Huet, J., Gobbo, A., Felisaz, F., Moya, R., McSweeney, S. M., Cusack, S., Cipriani, F. & Bowler, M. W. (2011). *J. Struct. Biol.* **175**, 236–243.
Russo Krauss, I., Sica, F., Mattia, C. A. & Merlino, A. (2012). *Int. J. Mol. Sci.* **13**, 3782–3800.
Sanchez-Weatherby, J., Bowler, M. W., Huet, J., Gobbo, A., Felisaz, F., Lavault, B., Moya, R., Kadlec, J., Ravelli, R. B. G. & Cipriani, F. (2009). *Acta Cryst.* D**65**, 1237–1246.
Scherer, M., Klingl, S., Sevvana, M., Otto, V., Schilling, E. M., Stump, J. D., Müller, R., Reuter, N., Sticht, H., Muller, Y. A. & Stamminger, T. (2014). *PLoS Pathog.* **10**, e1004512.
Scherer, M. & Stamminger, T. (2014). *Future Virol.* **9**, 415–430.

Schick, B. & Jurnak, F. (1994). *Acta Cryst.* D**50**, 563–568.
Sen, M., Yuki, K. & Springer, T. A. (2013). *J. Cell Biol.* **203**, 629–642.
Walter, T. S., Meier, C., Assenberg, R., Au, K.-F., Ren, J., Verma, A., Nettleship, J. E., Owens, R. J., Stuart, D. I. & Grimes, J. M. (2006). *Structure*, **14**, 1617–1622.
Weiss, M. S. & Hilgenfeld, R. (1999). *Acta Cryst.* D**55**, 1858–1862.
Wilkinson, G. W., Kelly, C., Sinclair, J. H. & Rickards, C. (1998). *J. Gen. Virol.* **79**, 1233–1245.
Winn, M. D. *et al.* (2011). *Acta Cryst.* D**67**, 235–242.
Wukovitz, S. W. & Yeates, T. O. (1995). *Nature Struct. Mol. Biol.* **2**, 1062–1067.